A&A 382, 1021–1031 (2002)
DOI: 10.1051/0004-6361:20011680

Astronomy & Astrophysics

Near-infrared Fabry-Perot imaging of Herbig-Haro energy sources: Collimated, small-scale H_2 jets and wide-angled winds

C. J. Davis[1], L. Stern[1,2], T. P. Ray[3], and A. Chrysostomou[4]

[1] Joint Astronomy Centre, 660 North A'ohōkū Place, University Park, Hilo, Hawaii 96720, USA
[2] Dept. of Physics, University of Victoria, PO Box 3055 STN CSC, Victoria, BC V8W 3P6, Canada
[3] Dublin Institute for Advanced Studies, School of Cosmic Physics, 5 Merrion Square, Dublin 2, Ireland
[4] Department of Physical Sciences, University of Hertfordshire, Hatfield, Herts AL10 9AB, UK

Received 17 September 2001 / Accepted 23 November 2001

Abstract. To search for further evidence of H_2 line emission towards the central engines of Herbig-Haro (HH) flows we have obtained near-infrared Fabry-Perot images of eight Class I outflow sources (SVS 13 [HH 7-11], L 1551-IRS5, HH 26-IRS, HH 72-IRS, SSV 63E [HH 24C], SSV 63W [HH 24J], HH 34-IRS and HH 111-IRS) and two Class 0 sources (HH 24-MMS and HH 25-MMS). Elongated H_2 emission (on scales of a few arcseconds) is detected from four of the Class I YSOs. These small-scale "jets" are associated with the base of more extended, parsec-scale HH outflows (and the "Molecular Hydrogen Emission Line" regions, or MHELs, discussed in Davis et al. 2001). In L 1551-IRS 5 we detect *two* jet components in H_2; these may be the molecular counterparts of the two known optical jets from this binary protostellar system, or they may represent H_2 excitation along the walls of a narrow, edge-brightened cavity. In addition to the small-scale MHEL jets, analysis of the data also suggests the presence of discrete molecular shock fronts formed along the jet axes close to the energy sources. In the most clear-cut example, SVS 13, we see an H_2 knot at a distance of about 440 AU from the outflow source; assuming a flow velocity of $\sim$200 km s^{-1}, then the dynamical age of this molecular feature is only 10 yrs. In these data we also see evidence for both collimated jets and wide-angled winds from the same sources. Indeed, even in one of the two Class 0 sources, HH 25MMS, a poorly-collimated flow component seems to be present. A two-component wind model may therefore be appropriate for outflows from Class I (and possibly even Class 0) protostars.

Key words. interstellar medium: jets and outflows – stars: pre-main-sequence – Herbig-Haro objects

1. Introduction

Although much is known about bipolar jets from protostars on large scales, their structure within a few arcseconds (<1000 AU) of their central engines is only now being explored. High-resolution optical *HST* images trace Herbig-Haro (HH) jets to within 100 AU of the driving source (e.g. Ray et al. 1996), while spectroscopic studies reveal blue-shifted jet components on scales of a few tens to a few hundred AU towards the same sources (e.g. Hirth et al. 1994a, 1997; Hirth et al. 1994b; Corcoran & Ray 1998; Bacciotti et al. 2000; Takami et al. 2001). This optical emission is excited at the base of HH jets from T Tauri (or Class II) protostars. Similar molecular line emission regions have recently been discovered towards a number of much younger, more deeply embedded, Class I sources, via spectro-astrometric observations of H_2 1-0 S(1) line emission (Davis et al. 2001 – Paper I). Davis et al. refer to these H_2 emission regions as "Molecular Hydrogen Emission-Line" regions, or MHELs, and compare their properties to those of Forbidden Emission-Line regions (FELs) observed in classical T Tauri stars. Like the FELs, both low- and high-velocity components (LVC and HVC) are observed in H_2; blue-shifted velocities of the order of 5–20 km s^{-1} and 50–150 km s^{-1} are measured respectively. LVCs are more common than HVCs in the MHEL regions observed, and like their FEL counterparts, HVCs are spatially further offset from the exciting source than LVCs. The MHEL regions are in all cases preferentially blue-shifted.

To complement these near-IR echelle data we have since sought high-spectral-resolution Fabry-Perot (FP) imaging of four of the Davis et al. sample of Young Stellar Objects (YSOs); two other Class I outflow sources and two Class 0 sources were also observed. The more extended regions of the MHEL features identified in Paper I are imaged directly with the FP (the MHEL regions within $\sim$1″ of each near-IR source are not distinguished from the continuum emission). These H_2 regions appear as 1″–5″–long extensions associated with each outflow source. They are distinct from the well-known HH knots and bow shocks

Send offprint requests to: C. J. Davis,
e-mail: c.davis@jach.hawaii.edu

seen on larger-scales further downwind, so we refer to them as "small-scale MHEL jets". In reality, however, the H_2 is associated with the base of a much larger (parsec-scale) molecular outflow in each case.

2. Observations

Data were obtained at the UK Infrared Telescope (*UKIRT*) with the facility near-IR imager *UFTI* between 22 and 24 November 2000. A Queensgate 50 mm diameter Fabry-Perot etalon was used in conjunction with *UFTI* to isolate line emission from continuum and scattered light near to each outflow source. The etalon has a plate spacing of 40 μm, a finesse of approximately 25 across the *K*-band, and a nominal resolution with *UFTI* of 400($\pm$20) km s^{-1} when properly aligned. Approximately the central 70″ circular diameter field of the *UFTI* array is unvignetted. The phase shift between the centre and edge of this area is $\sim$70–100 km s^{-1}; within a radius of 17″, the phase shift was measured to be only 35($\pm$5) km s^{-1}. Thus, one setting of the FP plate spacing is sufficient to accurately image an unresolved line across the entire unvignetted field. For the same reason sky OH lines are either transmitted or rejected across the whole field. The separation of adjacent orders corresponds to $\mathrm{d}\lambda/\lambda \sim 0.027$; hence, it is possible to use narrow-band (1%–2%) filters as "order-blockers".

Alignment of the FP plates (the *X* and *Y*, or "tip" and "tilt" axes) was carried out during the afternoon, just before the first night of observing. The FP was repeatedly tuned to the 2.11712 μm line of a krypton lamp by scanning through FPZ (the plate separation) at fixed values of *X* and *Y*. The *X* and *Y* values which gave the strongest lamp-line signal and narrowest (in plots of FPZ against flux) lorenzian profile were identified and subsequently used throughout the 3-night observing run. The tuning of the plate spacing (FPZ) to a given wavelength is, however, known to be temperature-sensitive. The FPZ value of peak transmission increases by about 30 km s^{-1} per °C drop in temperature. Thus, the initial values of FPZ measured at the beginning of each night (with *X* and *Y* set to their nominal values) needed to be checked and modified as the dome and ambient (outside) temperature dropped after sunset.

On each night, approximate values of FPZ were first used to infer the FPZ value for the H_2 1-0 S(1) line; these were used for sky-flat-field observations (where eight 200 second jittered exposures of twilight sky were median averaged and normalised). By the time the sky flat – which was deemed insensitive to small changes in FPZ – had been obtained, the dome and ambient temperature had essentially equalised (to within a degree) and stabilised to within 2–3 °C of the mean night-time temperature. This rapid thermal stabilisation is largely due to the *Dome Ventilation System* now in regular use at *UKIRT*. After the sky-flat observations, the FPZ tuning was again measured (using the krypton lamp) and this value used to infer the FPZ value specific to the $\lambda_{\mathrm{vac}} = 2.1218334\,\mu$m H_2 1-0 S(1) line (Bragg et al. 1982), for use with the first target. The dome temperature was subsequently monitoured throughout the night; following any changes in temperature (by more than 1–2 °C) FPZ was re-tuned with the krypton lamp, although we found that the tuned value never changed by more than 35–70 km s^{-1}.

Nine outflow regions were observed. Alternate on-line, off-line (blue-shifted), on-line and off-line (red-shifted) FPZ settings were observed, with the off-line FPZ settings offset by $\sim$800 km s^{-1} (roughly twice the FP profile *FWHM*). This four-frame sequence was repeated at 5 jittered positions on each source. The on-line and off-line images were dark-subtracted and flat-fielded separately, before being registered and combined into a "line+continuum" and a "continuum" image of each region. Since 120 s exposure times were used, each image represents a total of 20 min of on-source integration. For each target, either the line+continuum or the continuum image was lightly smoothed with a Gaussian weighting function (in an attempt to match the point-spread-function in the two mosaics) before the continuum image was subtracted from the line+continuum image to give the "H_2 S(1)" image. Note that the HH knots were in all cases absent from the continuum frames; this is testament to the accuracy and stability of the FP calibration.

Flux standards were also observed during each night. However, conditions were generally not photometric, so here we have simply normalised the mean flux measured across the same field stars present in the line+continuum and continuum images of each region.

3. Results

3.1. Small-scale H_2 jets from Class I outflow sources

High spectral resolution images, in H_2 1-0 S(1) line emission, were obtained of nine outflow source regions; the data for seven of these are presented in Figs. 1–3. Both Class 0 and Class I sources were observed. Line emission was detected from within a few arcseconds of the low-mass Class I sources SVS 13 (HH 7-11), L 1551-IRS 5, HH 26-IRS and the high-mass source HH 72-IRS. No line emission was detected towards the HH 34-IRS or HH 111 energy sources, nor towards the Class I YSOs SSV 63E and SSV 63W (which are associated with the "fan" of optical HH jets in HH 24). H_2 emission was observed towards the nominal positions of the deeply-embedded Class 0 sources HH 24-MMS and HH 25-MMS, although the association between each YSO and the H_2 emission is unclear (since the sources themselves are not detected in the near-IR; this is discussed in more detail below).

The FP images are presented as contour plots in Figs. 1–3; where complex line and continuum emission was detected the line+continuum mosaic is plotted alongside the "continuum-subtracted" H_2 S(1) image, i.e. the difference of the on-line and off-line mosaics. Diffuse nebulosity, already weak because of the very narrow bandpass of the FP etalon as compared to broad and even narrow-band filters, is largely removed in the H_2 S(1) images. Some

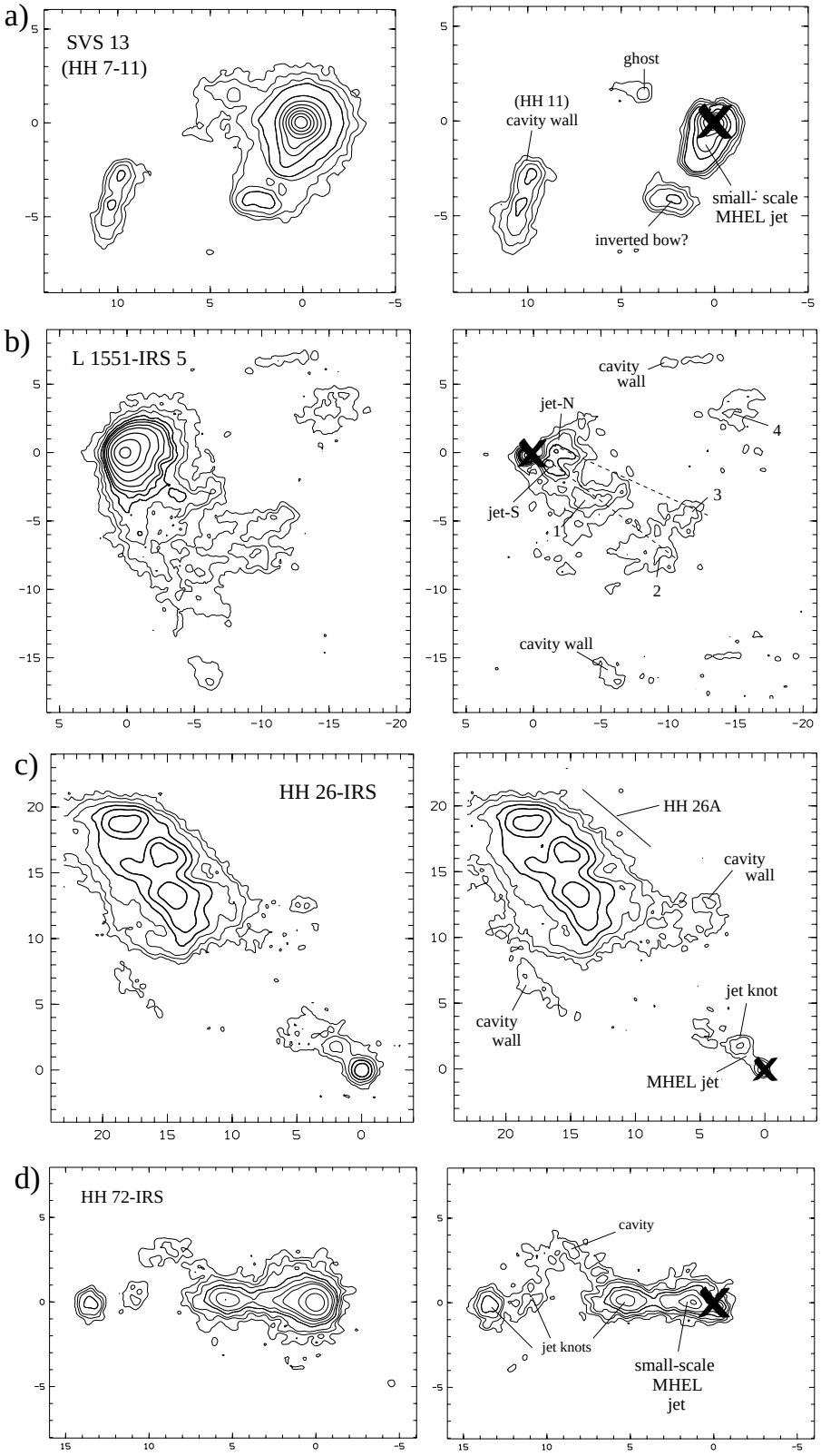

Fig. 1. H_2 line + continuum image (on-line; left) and H_2 S(1) image (on-line minus off-line; right) of four Class I outflow sources; SVS 13 (the HH 7-11 source), L 1551-IRS5, HH 26-IRS and HH 72-IRS. In each plot offsets are in arcseconds from the outflow source position. In the right-hand images, artifacts left over from the "continuum-subtraction" are masked with a 2″-diameter cross. The contours in the SVS 13 plots measure 5x, 7x, 10x, 14x, 18x, 45x, 64x, etc. the standard deviation to the mean background level. In L 1551-IRS5 the contours measure 3x, 5x, 7x, 10x, 12x, 15x, 22x, 32x, 64x, 128x and 256x the standard deviation to the background signal. In HH 26-IRS and HH 72-IRS they measure 4x, 8x, 16x, 32x etc. and 3x, 4x, 6x, 8x, 12x, 16x, 32x, and 64x the standard deviation, respectively.

residual emission remains in these difference images where bright, centrally-peaked stars are imperfectly subtracted. These artifacts are marked with a 2″-diameter thick cross in each figure; features covered by each cross are probably not real and should therefore be disregarded.

The three low-mass IR (Class I) sources, SVS 13, L 1551-IRS5 and HH 26-IRS, and the high-mass Class I YSO HH 72-IRS – which are all known to be associated with extensive molecular outflows – are shown in Fig. 1. In each flow, H_2 line emission was observed in the extended

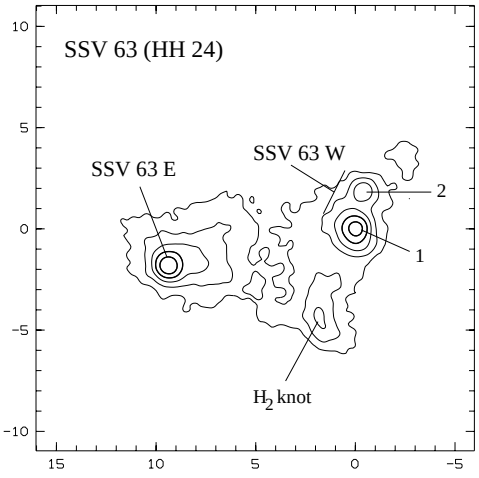

Fig. 2. FP line + continuum image of the SSV 63 region. The contours start at 4x the standard deviation to the mean background level and increase by factors of 2. Offsets are in arcseconds from the brighter component (1) of SSV 63W.

flows as well as directly towards the central source itself. The emission knots and bow shocks in these large-scale HH flows are well-known and described elsewhere (e.g. Hartigan et al. 1989; Chrysostomou et al. 2000; Davis et al. 1995, 1997), while the emission towards the outflow sources themselves has rarely been observed (Reipurth & Aspin (1997) present low-resolution *K*-band spectra of some of these sources). Echelle spectroscopy of the H_2 emission associated with SVS 13 and L 1551-IRS5 was discussed in Paper I; the small-scale "MHEL jet" towards HH 26-IR is newly-discovered.

In the echelle observations in Paper I the H_2 emission associated with SVS 13 was found to be particularly bright. The H_2 profiles comprise two velocity components, a low-velocity component (LVC) blue-shifted by about 25 km s^{-1} and a much higher-velocity component (HVC) blue-shifted by ∼100 km s^{-1}. In the FP data (Fig. 1a) the H_2 emission appears as an extension to the south-east of the IRS source; we identify this feature as being a small-scale MHEL jet. We do not distinguish the two velocity components in the FP images, however (though see the discussion in Sect. 4.1).

It is worth noting that the MHEL jet from SVS 13 might not be a jet at all. It could simply represent molecular emission excited along the walls of a wind-swept cavity. A broad cavity, which extends from SVS 13 to the bright HH 7 bow shock, is evident in deep optical and near-IR images of the HH 7-11 region (Davis et al. 1995; Chrysostomou et al. 2000). However, we consider this to be unlikey because: 1) the MHEL feature is not aligned with either cavity wall (in the H_2 images of Chrysostomou et al. the limb-brightened cavity walls extended almost precisely eastward and southward; the MHEL jet position angle in Fig. 1a measures ∼159°), 2) we only see one feature (rather than both cavity walls), 3) the MHEL jet is aligned with nearby HH objects and, notably, with the proper motion vectors of these HH objects (Chrysostomou et al. 2000), and 4) in Paper I we observed high radial velocities in the MHEL region; one would perhaps expect lower velocities if the H_2 were excited in a turbulent boundary layer between a wide-angled wind and a cavity wall.

In Fig. 1a there is a break in detected H_2 line-emission between the small-scale SVS 13 molecular jet and the rest of the observed outflow. The arc of H_2 emission found ∼5″ to the south-east of SVS 13 may be caused by the unseen flow impacting a stationary or slow-moving clump here, since the arc curves away from the source. This "inverted bow shock" and the small-scale H_2 jet share a common axis (to within a few degrees) with HH 8, 10 and 11B further downwind.

In L 1551-IRS 5 the subtraction of the continuum emission reveals two near-parallel jet-like features, labelled jet-N and jet-S (Fig. 1b). The two jets could be associated with the two velocity components identified in the H_2 echelle data in Paper I; in these echelle data a near-stationary H_2 component extends as far as a bright optical bow shock seen 10″–12″ downwind of the source (Fridlund & Liseau 1998; Hartigan et al. 2000), while a second, "accelerating" H_2 component extends only about half as far downwind. The two features – jet-N and jet-S – are also probably the H_2 counterparts of the two "jets" seen in the optical imaging of Fridlund & Liseau (1998) and Hartigan et al. (2000), and recently in near-IR [FeII] emission by Itoh et al. (2000). In the optical the two jets appear to be diverging at an angle of ∼20°. The H_2 jets behave in a similar way; the position angles (p.a.) of jet-N and jet-S measure 260°(±2°) and 244°(±2°) respectively. Itoh et al. (2000) report angles of ∼250 − 280° for jet-N and ∼230–260° for jet-S (they suggest that the jets could be twisting along their lengths, hence the range in angles; also, the jets appear more extended in the optical and [FeII] images).

Alternatively, jet-N and jet-S (and their optical counterparts) could again represent the walls of a very narrow, edge-brightened cavity associated with a single, unseen jet (Mundt et al. 1991). However, in Paper I we measure radial H_2 velocities that are blue-shifted by up to 60–70 km s^{-1}, while in the optical radial velocities approaching 300 km s^{-1} have been observed (Hartigan et al. 2000). As with SVS 13 one might expect lower radial velocities if the emission were associated with such a boundary layer.

Jet-N and jet-S both pass through faint H_2 features downwind (as indicated by the dashed lines in Fig. 1b); we detect more H_2 emission along the southern jet axis which, notably, is the fainter and slower component at optical wavelengths (Hartigan et al. 2000). The axis of the 1.2″-wide echelle slit (PA = 66° E of N) used in Paper I, which was centred on the bright IRS continuum peak, passed along the southern jet axis though through the H_2 feature labelled 3 here in Fig. 1b. We therefore associate jet-S and knot 1 with the accelerating H_2 component identified in Paper I. The double-peaked H_2 profile observed 10–12″ away from the IRS 5 peak could then be associated with

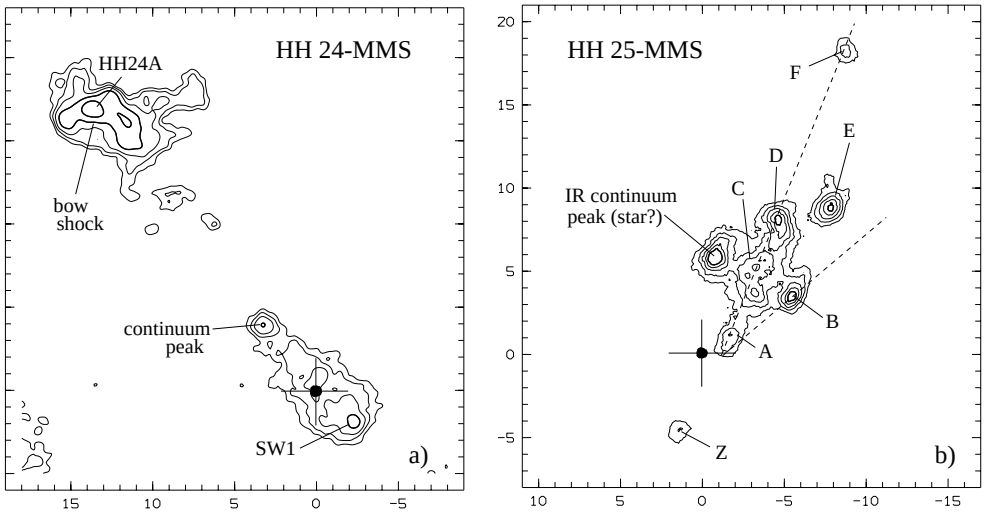

Fig. 3. FP line+continuum images of the Class 0 sources HH 24-MMS and HH 25-MMS. The contours for HH 24-MMS measure 5x, 7x, 10x, 16x, 32x the standard deviation to the mean background level; for HH 25-MMS they measure 3x, 4x, 5x, 6x, 7x the standard deviation. The crosses mark the positions of the two embedded sources. The IR continuum peak at offsets $(-1'', 6'')$ in b) is probably an unrelated background star.

knot 3 in Fig. 1b and the HH bow shock seen by Fridlund & Liseau (1998), Itoh et al. (2000) and Hartigan et al. (2000).

The FP observations of HH 26-IRS and HH 72-IRS are also shown in Fig. 1. In the former, the newly-discovered MHEL jet associated with the source is manifest as a slight extension of the source profile in the line+continuum image. This extension is perfectly aligned with the axis that links the IRS source with a nearby jet knot (labelled in Fig. 1) and the much brighter, more extended H_2 shock features that comprise HH 26A further downwind. By comparison, in the more distant, high-mass HH 72 outflow, the MHEL jet associated with the near-IR outflow source is far more distinct. Again, this small-scale jet is closely aligned with HH features seen further along the larger-scale HH outflow axis.

3.2. Unresolved or undetected molecular jets

The Class I YSOs SSV 63E and SSV 63W (Zealey et al. 1992) are associated with at least two parsec-scale, bipolar HH jets which form part of the HH 24 complex (Solf 1987; Mundt et al. 1991; Eislöffel & Mundt 1997). SSV 63E is possibly the exciting source of the HH 24 C jet, while SSV 63W may power HH 24 J. Davis et al. (1997) present narrow-band near-IR images of the region which resolve SSV 63W into two stars. These two sources, separated by $1.9''(\pm 0.7'')$, are also evident here in Fig. 2. We see no clear evidence of small-scale MHEL jets associated with either SSV 63E or SSV 63W. However, there is a "finger" of H_2 emission $5''$–$6''$ south of SSV 63W. This H_2 feature is coincident with the second-brightest HH object in the region, HH 24B, although it does not lie on any of the principal optical jet axes identified by Eislöffel & Mundt (1997).

Like SSV 63E and W, the Class I source HH 34-IRS powers a highly-collimated optical jet (Eislöffel & Mundt 1992; Bally & Devine 1994; Ray et al. 1996), and like the SSV 63 sources, no small-scale MHEL jet was evident in our FP data (not shown here). However, HH 34-IRS was included in the near-IR echelle observations in Paper I, where line emission was detected towards the source. The H_2 emission was found to be coincident with the source continuum position, to within a spectro-astrometric measurement error of $0.12''$. The HH 34 outflow is thought to be orientated at about 30° to the plane of the sky. The H_2 line emission observed in Paper I must therefore be produced in a region very close to the central source. Indeed, from the *FWHM* of a 2-D Gaussian fit to the source profile we set an upper limit of $0.79''$ to the extent of any MHEL jet that might be associated with HH 34-IRS (this is equivalent to a de-projected length of 460 AU, assuming a distance of 450 pc to this source). Echelle spectroscopy of SSV 63E and SSV 63W would be interesting to test whether spatially-unresolved H_2 is also excited coincident with these other, similar, Class I sources, sources which (like HH 34-IRS) are thought to drive large-scale HH outflows.

The FP images of the two Class 0 sources observed, HH 24-MMS and HH 25-MMS (Bontemps et al. 1995; Gibb & Davis 1998), are presented in Fig. 3. The locations of these embedded millimeter sources are marked in each figure: their positions are derived from a comparison of the wide-field near-IR mosaics of Davis et al. (1997) with optical and near-IR astrometry obtained from the *HST Guide Star Catalogue* and the *2MASS* on-line databases. Since only seven, relatively nebulous IR sources were common to these datasets, the astrometry is accurate to only $\sim 2''$–$3''$; this level of accuracy is indicated by the crosses in Fig. 3. The coordinates used for HH 24-MMS and HH 25-MMS were taken from the 3.6 cm VLA observations of Bontemps et al. (1995) where the synthesized beam of the VLA was $\sim 10''$. Source confusion within this beam may result in uncertainties in these positions of the order of a few arcseconds. The true location of each driving source may therefore be closer to the two jet axes than indicated (and the HH 24-MMS source could be closer to the faint continuum peak). Indeed, more recent 350 μm and 1300 μm imaging of HH 25-MMS (which is extended in the 3.6 cm map of Bontemps et al.) indicates the presence of two unresolved sources, with the colder source offset a few arcseconds to the south of the warmer source and VLA position

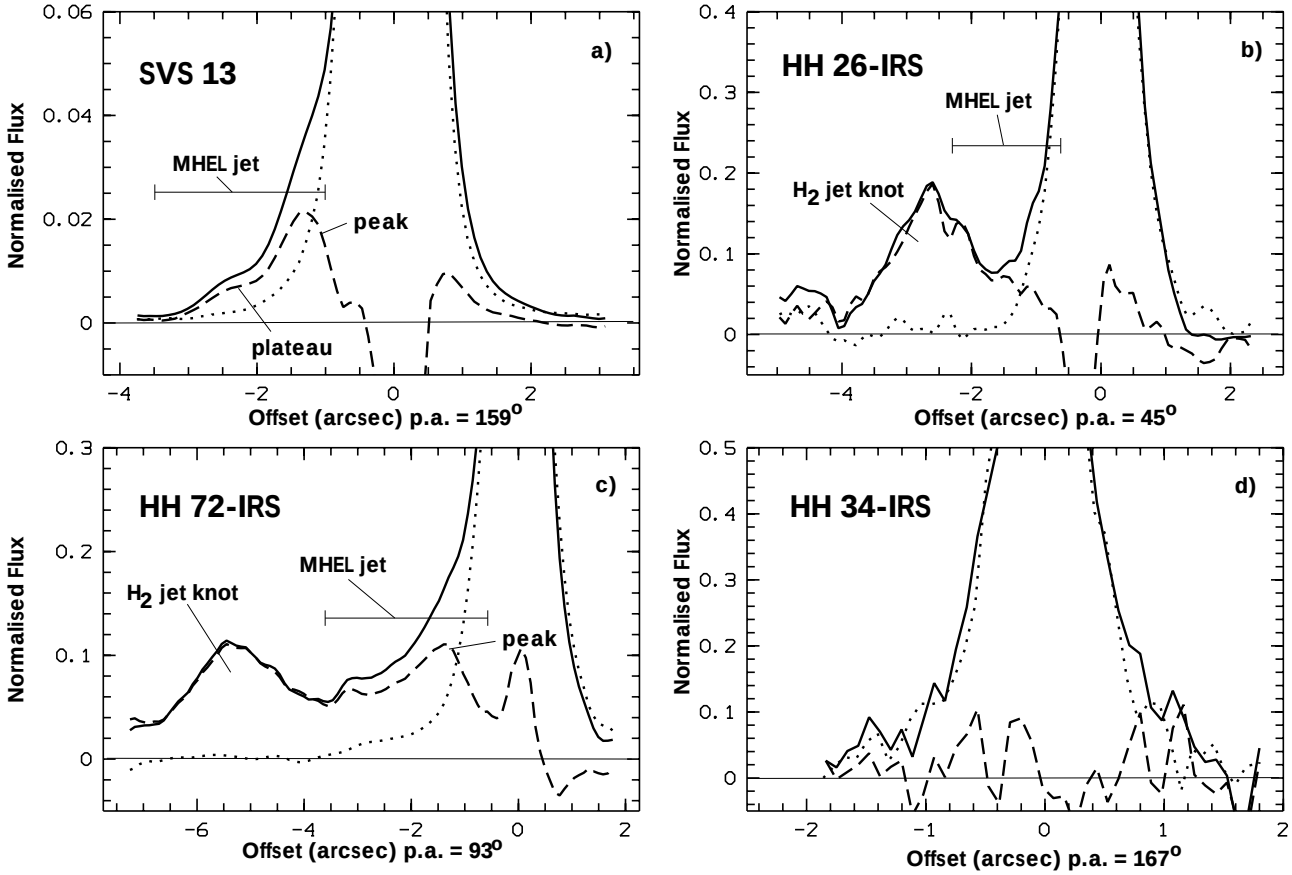

Fig. 4. Intensity profiles along each MHEL jet axis (full line) and perpendicular to it (dotted line); both plots were centred on the near-IR source position (arcsecond offsets are from this position). The dashed line shows the difference of the two profiles; this represents the distribution of line emission along the jet axis. Offsets are from the near-IR source position. The intensity scale is normalised to the peak flux in each source.

marked here in Fig. 3b (Lis et al. 1999). The HH 25-MMS jet source could therefore be midway between the H_2 knots A and Z, with the warmer, less deeply embedded component associated with the near-IR continuum peak.

Our FP images of HH 24-MMS and HH 25-MMS show H_2 emission associated with both jet axes, although since neither source is observed directly we claim no detection of a small-scale MHEL jet akin to those described above. Knot SW1 in HH 24-MMS is probably a curved bow shock driven by the underlying jet; HH 24A in the counterflow is a much brighter optical/near-IR bow shock that may be associated with either the HH 24-MMS flow or the orthogonal HH 24C jet (PA $\sim$ 150°) from SSV 63E (discussed in detail by Eislöffel & Mundt (1997) and Davis et al. (1997)). HH 25-MMS, on the other hand, seems to be associated with a cone of H_2 knots (illustrated by the dashed lines in Fig. 3b; the H_2 knots are labelled A–F). The faint knot Z is probably a knot in the red-shifted counterflow (Gibb & Davis 1998).

Finally, FP images of the HH 111 source region were also secured. However, the faint near-IR source of this bipolar HH jet (Reipurth et al. 1999) was not detected. Nor were any H_2 knots within $\sim$20″ of the central source position; these data are therefore not presented.

4. Discussion

4.1. Small-scale, collimated jets from YSOs

Precisely subtracting the stellar-continuum point-spread-function (PSF) from the FP images of each outflow source is hampered by the fact that, in most of the fields observed, there were few (or no) other field stars for PSF-matching, relative flux-scaling, or image registration. To more clearly display and more accurately disentangle the H_2 emission features and small-scale MHEL jets from their central energy sources we therefore plot in Fig. 4 intensity cuts made along (and orthogonal to) the jet axes of three of the Class I sources (SVS 13, HH 26-IRS and HH 72-IRS). Similar cuts made through a fourth Class I YSO, HH 34-IRS (where no small-scale jet extension was observed), are also shown for comparison. In each case, the line+continuum image was rotated so that the jet axis was orientated along rows in the image. Gaussian fits to cuts made orthogonal to the jet axis at between six and 12 locations along each small-scale jet were made to confirm that the angle of rotation was within a degree of the nominal MHEL jet axis (precise jet position angles are listed in Table 1). Five-pixel-wide "strips" were then extracted from each rotated image and the data binned along the

Table 1. Small-scale H_2 jet and wide-angled wind parameters.

Target	Source class	MHEL jet p.a.[1] (° E of N)	PSF[2] (arcsec)	$\alpha^3_{\rm MHEL}$ (arcsec)	θ^4 (degs)	$L^5_{\rm MHEL}$ (AU)	Opening angle of MHEL jet (degs)	Opening angle of wide-angled wind (degs)
SVS 13 (HH 7-11)	Class I	158.9(±0.5)	0.61(±0.04)	<2.6	40	<890	<24	95(±4)
L 1551-IRS 5 jet-N	Class I	259.5(±2.0)	0.65(±0.1)[6]	∼ 3.9	45	∼ 800	<14	99(±4)[7]
L 1551-IRS 5 jet-S	Class I	244.1(±2.1)	0.65(±0.1)[6]	∼ 3.4	45	∼ 700	<20	99(±4)[7]
HH 26-IRS	Class I	42.2(±4.1)	0.94(±0.1)	<4	∼90	<1800	–	52(±5)
HH 72-IRS	Class I	94.1(±2.3)	0.81(±0.2)	<4.8	∼90	<7200	<27	39(±3)
HH 34-IRS	Class I	–	0.79(±0.1)	<0.9	60	<460	–	–
HH 24-MMS	Class 0	–	–	–	–	–	–	<26[8]
HH 25-MMS	Class 0	–	0.80(±0.15)[6]	–	∼ 90	–	–	28(±5)

[1] Small-scale MHEL jet position angle, measured from Gaussian fits to cuts made orthogonal to the jet axis at 6–10 locations along each jet. A binned line+continuum image was used in each case, except for L 1551 where the continuum-subtracted $H_2S(1)$ image was used. Values also take into account the orientation of the *UFTI* array on the sky.
[2] Measured from 2-D Gaussian fits to field stars in each mosaic.
[3] Angular extent of the MHEL jet on the sky (i.e. not de-projected).
[4] Inclination angle of the outflow with respect to the line of sight.
[5] Length of the small-scale MHEL jet, corrected for flow inclination angle, θ. For SVS 13, HH 26-IRS and HH 72-IRS upper limits are derived from intensity cuts made along the jet axis (see Fig. 4). For L 1551 the distance from the IR continuum peak to a point in each jet where the H_2 emission drops to ∼50% its peak value (in that jet) is given. For HH 34, the PSF measured for the source itself is used as an upper limit. Distances of 450 pc are assumed for HH 25-MMS, HH 26-IRS and HH 34-IRS; 220 pc for SVS 13; 150 pc for L 1551-IRS 5; and 1500 pc for HH 72-IRS.
[6] PSF based on observations of standard stars taken before and after the observations of the target.
[7] Wide-angled wind associated with the L 1551-IRS 5 flow overall; see Fig. 1b.
[8] Measured between knot SW1 and the continuum peak; see Fig. 3a.

minor axis in each image. The resulting 1-D images were finally registered so that profiles along and perpendicular to each jet axis could be plotted together. The profiles perpendicular to the jet axes essentially represent the underlying stellar PSF of the jet source and any associated nebulosity; the difference of the parallel (full) and perpendicular (dotted) plots, which is drawn with a dashed line in Fig. 4, then illustrates the distribution of H_2 line emission close to the central IR peak.

In Fig. 4a the small-scale MHEL jet associated with SVS 13 is seen as a distinct wing on the south-eastern side (i.e. negative offsets) of the SVS 13 continuum PSF. This continuum-subracted H_2 profile (the dashed line in Fig. 4a) appears to consist of a peak superimposed onto a more extended plateau. These two spatial components may be associated with the two dynamical components seen in the echelle data in Paper I (where an LVC at $V_{\rm LSR} \sim -20\,{\rm km\ s^{-1}}$ and a fainter HVC at $V_{\rm LSR} \sim -100\,{\rm km\ s^{-1}}$ are observed). Since the LVC is more extended than the HVC in the echelle data, it is tempting to associate the LVC with the plateau in Fig. 4a, and the HVC with the peak nearest the source. However, the *peak* of the HVC in the echelle data is further offset from the source than the LVC peak, which is the opposite of what we see in the FP data. Note also that the HVC and LVC peaks in the echelle data are found within a few tenths of an arcsecond of the continuum peak; we are not able to extract information on such fine spatial scales, or indeed so close into the central YSO, from the FP data.

We therefore associate the plateau in the H_2 profile with the overall MHEL jet (and probably predominantly the brighter and more extended LVC in the echelle data) and postulate that the "peak" in Fig. 4a could be associated with a more discrete shock front formed along the jet axis. This shock front could be due to a recent ejection event. If we disentangle the peak from the plateau via a two-component Gaussian fit to the continuum-subtracted H_2 profile, then the peak is found to occur at an offset of $-1.28''(\pm 0.01'')$ from the central source (the plateau is offset by $-2.13''[\pm 0.09'']$). Assuming a distance of 220 pc to SVS 13 and a flow inclination angle of 40° to the line of sight, then the offset of the peak along the jet axis measures 435 AU. If we also assume a flow velocity of ∼200 km s^{-1} (Chrysostomou et al. 2000), then the dynamic age of this shock front is only about 10 yrs. The extent of the plateau component in Fig. 4a also gives a rough upper limit to the length of the SVS 13 MHEL jet. If we adopt twice the *FWHM* of the Gaussian fit to the plateau component described above as the jet length, then we arrive at a value of $<2.6''(\pm 0.2'')$, equivalent to <890 AU after correction for the flow inclination angle. Together, the peak and plateau components suggest the presence of a molecular shock front at a distance of only ∼450 AU from the source, situated roughly half-way along the length of a 900 AU-long MHEL jet.

The small-scale H_2 jet associated with HH 26-IRS is less clearly resolved. Weak line emission is seen at negative offsets in Fig. 4b within $\sim 2''$ of the source. This

extended emission runs into the H_2 jet knot identified in the contour plot in Fig. 1c. Beyond $4''$ from the source we see no evidence of the jet. We therefore adopt $4''$ as an upper limit to the HH 26-IRS jet length in Table 1.

In HH 72-IRS the first H_2 jet knot is again evident as a peak in the continuum-subtracted H_2 intensity profile (Fig. 4c). The emission associated with the MHEL jet peaks within $2''$ of the source and extends out as far as the H_2 knot. A three-component Gaussian fit to the continuum-subtracted H_2 profile suggests the presence of a broad, $FWHM = 2.4''(\pm 0.4'')$-wide component (peaking at $-2.6''[\pm 0.2'']$) linking the two more distinct, though narrower peaks at offsets of $-5.25''(\pm 0.02'')$ and $-1.40''(\pm 0.01'')$. The peak at $-5.3''$ represents the jet knot labelled in Fig. 1d; the peak at $-1.4''$ may be a similar, discrete shock front along the jet axis, though one formed much closer to the source. Both peaks may then be superimposed onto the broader, underlying MHEL jet component.

The echelle data for HH 72-IRS in Paper I suggest the presence of LVCs ($V_{\rm LSR} \sim 0{-}80\,{\rm km\ s^{-1}}$) offset by $0.6''$–$1.0''$ from the source, with a more extensive HVC ($V_{\rm LSR} \sim 150\,{\rm km\ s^{-1}}$) peaking further downwind at an offset of $2''$–$4''$. Much of the MHEL jet emission seen with the FP is therefore probably associated with the higher-velocity emission. We estimate a very crude upper-limit to the small-scale MHEL jet length, equivalent to twice the $FWHM$ of the broad component ($\sim 4.8''$) in the multicomponent fit, of 7200 AU (we assume that the flow lies in the plane of the sky). We then estimate a distance for the shock front nearest the source of about 2100 AU. Given a flow velocity of 200 km s^{-1}, similar to that derived for the more intensely-studied SVS 13/HH 7-11 outflow (see above), then the dynamical age of the first H_2 knot in the HH 72-IRS flow is only $\sim$50 yrs.

The remaining plot in Fig. 4d reitterates the fact that the H_2 line emission found coincident with HH 34-IRS in the echelle spectroscopy in Paper I is also spatially unresolved along the jet axis in the FP data. The intensity profile along the jet axis (as defined by larger-scale optical images of the more extended HH flow; e.g. Ray et al. 1996) matches precisely with that taken perpendicular to the jet.

In Table 1 we list estimates (in some cases upper limits) for the length of each small-scale MHEL jet observed. The angular extent of the jet is given alongside the deprojected size in AU. The orientation of each flow with respect to the line-of-sight, θ, is also given (see Paper I for references to θ; see also Gibb & Davis 1998 and Gibb & Heaton 1993 for the HH 25 and HH 26 outflows). The small-scale jet lengths for SVS 13, HH 26-IRS, HH 34-IRS and HH 72-IRS are derived from the profiles in Fig. 4 (described above). (A value for HH 34-IRS is given since, although no small-scale jet extention was observed in these FP data, H_2 line emission was detected, coincident with HH 34-IRS, in Paper I.) Note also that the lengths of the jets in L 1551-IRS5 are with respect to the near-IR continuum peak position for IRS 5; specifically, we quote the distance between the end of each jet (where the H_2 flux drops to 50% its peak value seen in the continuum-subtracted image of the jet) and the IRS 5 continuum peak position in each case.

4.2. Wide-angled winds

In addition to the small-scale H_2 jets associated with some of the Class I sources observed, the FP data also reveal H_2 emission knots in the more extended outflow lobes. H_2 1-0 S(1) line emission in outflows almost exclusively derives from shock-excited ambient and/or jet material (Gredel 1994; Fernandes & Brand 1995; Eislöffel et al. 2000). In the dense, post-shock gas typically associated with molecular outflows, H_2 cooling times are very short, of the order of a few years (Shull & Hollenbach 1978; Smith & Brand 1990). Any observed H_2 features therefore illustrate current regions of shock-interaction (unlike other tracers, such as CO, which provide a fossil record of an outflow).

In the flows from all four Class I YSOs in Fig. 1 we see evidence of current H_2 shock-excitation along the walls of a wind-swept, wide-angled cavity. In the "younger" flow from the Class 0 source HH 25-MMS the H_2 features describe a cone rather than a collimated jet, although the opening angle of this cone of emission knots is somewhat narrower than the cavities observed in the Class I YSO outflows (a very similar cone of emission knots is seen in the molecular flow from the Class 0 source L 1448-IRS3; see e.g. Davis & Smith 1995). In HH 24-MMS, probably the youngest source observed (Lis et al. 1999), the south-western flow lobe may also be expanding, although we consider it more likely that the feature labelled SW1 in Fig. 3 is a bow shock driven by a highly collimated jet.

Wind-swept cavities have been observed on numerous occasions in the past, particularly when molecular emission-line maps of swept-up gas are compared with optical observations of hot, knotty HH jets. Perhaps one of the most striking examples is the HH 46/47 counterflow, where a collimated H_2 jet flows along the axis of a wide-angled cavity that is caped by an extensive, limb-brightened bow shock (Eislöffel et al. 1994). Indeed, extensive cavities have been observed in wide-field optical and near-IR images of many bipolar outflows, from both young Class I sources and more evolved T Tauri stars, as well as from low and high-mass stars; e.g. HH 7-11 and L 1551-IRS 5 (Graham & Heyer 1990; Davis et al. 1995), L 483 (Fuller et al. 1995), HH 195 (Eislöffel 2000), IRAS 06047-1117 (Yun et al. 2001), Cep A (Hartigan et al. 1996), V380 Ori (Corcoran & Ray 1995), V645 Cyg (Goodrich 1988) and MWC 1080 (Poetzel et al. 1992). In other systems, deep images reveal off-axis knots that must also be associated with cavities; in HH 1, for example, we see H_2 knots along one edge of what appears to be a shocked cavity wall, as well as line-emission from a highly-collimated partially-ionised/partially-molecular jet (Davis et al. 2000). In recent years, mm-wave interferometric CO

maps have also revealed broad shells of cool, molecular gas that are co-axial with well-known, collimated HH jets (e.g. Gueth et al. 1996; Mitchell et al. 1997; Lee et al. 2000). So wide-angled cavities are certainly a common phenomenon in protostellar outflows.

It has also been suggested that the opening angles of jets from YSOs increase with age (Velusamy & Langer 1998); the idea of changing opening-angles was discussed at length in an earlier paper on L 1551-IRS5 (Davis et al. 1995). There is some evidence to support these claims from the modest sample of sources discussed in this paper. Nevertheless, with the possible exception of HH 24-MMS, we do still see simultaneous evidence for a wide-angled wind component *in addition* to a collimated jet component aligned with the flow axis.

In Table 1 we give estimated flow opening angles, based on the angle subtended at each source by the H_2 features seen along the "cavity walls" in each system. For comparison, we also give estimated upper limits to the opening angles of each small-scale jet. The jet opening angles are derived from the ratio of the jet length to *FWHM* width measured at locations along the jet axis where the emission is still observed at the 5–10σ level. Since the jet may be longer (in more sensitive images) and the width is typically unresolved (the *FWHM* is equivalent to the seeing), the MHEL jet opening angles are very much upper limits.

In attempts to model HH jets and molecular (CO) outflows it has been noted that both jet-driven bow shock models (Raga & Cabrit 1993; Chernin et al. 1994) and wind-driven shell models (Shu et al. 1991, 2000) fail to produce certain observational traits. Jet-driven bow models produce molecular flow lobes that are often too narrow (at best an outflow lobe radius of 3–5× the underlying jet radius is predicted; Smith et al. 1997a; Downes & Ray 1999), while wide-angled wind models fail to produce the compact knots often observed along the jet axes of the same broad, molecular outflows (Mitchell et al. 1997; Lee et al. 2000). Since flow evolution, from a collimated jet to a wide-angled wind, cannot explain the presence of both a broad CO outflow and a collimated, knotty jet in the same source, a dual-component wind might instead be appropriate. Indeed, a magnetised radial wind should have an enhanced on-axis density (Shu et al. 1995; Shang et al. 1998) which, if combined with flow variability, might then explain many of the observed parameters of molecular flows from Class I YSOs in particular, where collimated (MHEL) jets *and* wide-angled winds and/or cavities traced in shock-H_2 emission seem to be common.

4.3. The origin of H_2 in MHEL regions and small-scale jets

The origin of the H_2 observed within a few hundred AU of the Class I protostars observed so far, either via the echelle spectro-astrometry in Paper I or via the FP imaging in this article, is not immediately obvious. H_2 molecules will be dissociated in strong shocks or an intense radiation field, so the survival and excitation of H_2 must to some extent constrain the condition in the region that excites the emission.

Firstly, does the H_2 emission derive from molecules reformed within a rapidly-cooling, atomic jet driven by the central engine? If we assume an H_2 reformation rate of $\sim 3 \times 10^{-17}\,\mathrm{cm^3\,s^{-1}}$, appropriate for reformation in a cold gas and dust environment (Hollenbach & McKee 1989), then given the 10 year dynamical age of the H_2 emission peak in the SVS 13 MHEL jet (derived in Sect. 4.1), a gas density of at least $\sim 10^8\,\mathrm{cm^{-3}}$ must be maintained in the cooling flow for H_2 to reform in time. This value for the density is however a lower limit, since we do not consider the time taken for the gas and dust to cool prior to the onset of reformation (the temperature in the flow must first drop to less than $\sim$500 K). Moreover, in Paper I high-velocity H_2 emission is observed much closer to the source in some outflows, on spatial scales of a few 10s of AU. A shorter dynamical time-scale is then inferred, and a gas density an order of magnitude higher would be needed to accomodate the rapid cooling and subsequent H_2 reformation.

Also, formation of H_2 in a sufficiently excited state to produce the strong H_2 1-0 S(1) emission observed in the small-scale MHEL jets is unlikely: Hollenbach & McKee (1989) predict 1-0 S(1) intensities of $<10^{-6}$ W m^{-2} sr^{-1} from formation and collisional pumping in the reformation region, which is a factor of at least 10 lower than is observed (Paper I; note that the measured fluxes are uncorrected for extinction). So the reformed H_2 would have to be excited into emission via some other, external means, either in a shock or via fluorescence from the central star.

Since it is unlikely that the H_2 has time to reform in the flow as it accelerates away from the disk surface, the observed H_2 in the small-scale jets imaged here and the MHEL regions discussed in Paper I must be excited and remain intact in the MHEL jet regions associated with each source. The high-velocity H_2 must be part of some disk wind component to each jet. Note that in many of the MHEL regions observed in Paper I, the H_2 emission (observed within 100 AU of the near-IR continuum source position) is accelerated to blue-shifted velocities of 10–30 km s^{-1}. If the H_2 represents stationary, ambient gas shocked by an atomic/ionic wind, one would expect to see emission at the systemic rest velocity. The H_2 must therefore be part of the wind itself. In other words, the wind from the central star and disk must be – at least in part – molecular. Internal shocks and/or fluorescence from the central source could then produce the observed emission.

Do high-energy continuum photons from the central protostar, or Lyα photons from hot shocked gas associated with accretion flows, excite H_2 into emission at the base of each jet? H_2 emission lines observed in the UV, which can only be excited via fluorescence, have been detected in a small number of T Tauri stars (Valenti et al. 2000). In a similar fashion fluorescent excitation of molecular material close to Class I sources may also be important. FUV

photons (6 eV $\leq h\nu \leq$ 13.6 eV) from the central protostar will penetrate along the jet beam further than they do in the orthogonal disk plane because of the lower gas density along the polar jet axis. Extinction may then block our view of fluoresced H_2 in the inner regions of a circumstellar disk (particularly in the edge-on systems). Along the jet axis, however, FUV photons will excite H_2 out to a distance of about $1A_v$ (Burton et al. 1990). Given the MHEL jet lengths (and upper limits) listed in Table 1, we can estimate at least an upper limit to the mean gas density along the jet axis if FUV pumping is the dominant excitation process. For H_2 pumping out to a distance of about 1000 AU – the typical MHEL jet length – the mean gas density along the jet must be about $10^5\,cm^{-3}$. Shorter jet lengths imply higher jet densities. Notably, jet densities of the order of $\sim 10^4\,cm^{-3}$ are usually measured for HH jets on larger,"tens-of-arcsecond" scales (e.g. Bacciotti & Eislöffel 1999); at these radial distances the jet will have undergone some lateral expansion, so higher jet densities are likely closer to the central engines, in the MHEL regions.

However, to produce the strong 1-0 S(1) intensities reported in Paper I, slab-PDR models predict that a strong local FUV radiation field ($\geq$0.1 W m^{-2} [$G_o \geq 10^5$] when summed across the wavelength range 913–2069 Å) and a high gas density ($\geq 10^5\,cm^{-3}$) are needed (Burton et al. 1990; Hollenbach & Natta 1995), particularly for SVS 13, L 1551-IRS5 and the high-mass source HH 72-IRS where the H_2 surface brightness is high, $\sim 0.5-1 \times 10^{-5}$ W m^{-2} sr^{-1}. Typical UV continuum luminosities of $10^{22}-10^{23}$ W $Å^{-1}$ have been measured in T Tauri stars (Johns-Krull et al. 2000). Given an average separation of about 500 AU between each MHEL jet and the outflow source/accretion zone (and after multiplying the luminosity by the wavelength range $\Delta\lambda = 1156$ Å), then these FUV continuum luminosities are still 2–3 orders of magnitude below the values required by the slab-PDR models. Lyα photons from accretion shocks in T Tauri stars could also contribute to the H_2 pumping, although Lyα fluxes may be even lower (e.g. Blondel et al. 1993). Of course, from Class I protostars FUV intensities may be higher than quoted here for T Tauri stars, since mass accretion rates are higher, although extinction effects will also probably be greater. Moreover, the high gas densities required by the PDR model would limit the extent of the PDR – and so the small-scale MHEL jet length – as noted earlier. It seems unlikely, then, that FUV pumping is the dominant excitation mechanism in the MHEL regions observed, although careful analysis of the excitation of the MHEL regions is clearly of considerable interest.

Finally, could the H_2 emission be produced in internal shocks, resulting from episodic ejections or flow variability? The relatively high radial velocities measured in Paper I testify to excitation in the flow rather than the surrounding medium or along the edges of a flared disk. Slowly varying jet velocities (and jet directions) have been invoked to explain the fast-moving chain of bow shocks often seen on tens-of-arcsecond scales in HH flows and molecular jets like HH 111 and HH 212 (e.g. Raga & Biro 1993; Smith et al. 1997b; Völker et al. 1999). Inter-knot spacings of less than an arcsecond (< few hundred AU) are observed in some of these extended flows (e.g. Ray et al. 1996; Reipurth et al. 2000), particularly in the jet sections closest to the central source. Given jet velocities of a few hundred $km\,s^{-1}$, these inter-knot distances imply variability time scales of the order of 5–50 years. The close proximity of the MHEL regions to their central engines imply ejection or variability time scales of perhaps an order of magnitude less than this. Clearly, we do not have the spatial resolution to investigate whether small-scale MHEL jets are continuous or "knotty" on milliarcsecond scales, so we can not test this hypothesis directly. We do mention, however, that the MHEL features seem dynamically and morphologically unrelated to the larger-scale H_2/HH objects seen further downstream in most of the flows studied so far (i.e. they possess different velocities and appear spatially disconnected). The mechanisms that excite the emission from the MHEL jet regions and the HH objects further downwind could therefore be quite different.

5. Conclusions

FP images are used to illustrate the H_2 line emission within a few arcseconds of young HH energy sources. In all, 10 outflow sources have been observed. We see evidence of emission – in the form of a small-scale molecular jet – from four Class I sources. These "MHEL jets", apparent as extensions to the source PSF in each source, are aligned with the larger-scale flow axes and the proper motion vectors of HH knots seen further downwind.

Analysis of the FP data reveal the presence of H_2 knots within a few hundred AU (in SVS 13) and a few thousand AU (in the more distant high-mass YSO HH 72-IRS) of the central outflow source. Given reasonable estimates for the flow inclination angle and on-axis flow velocity, the dynamical ages of these molecular shock fronts are of the order of 10 yrs and 50 yrs respectively. High (sub-arcsecond)-resolution spectro-astrometry would be of use for disentangling the spatial MHEL jet components in these sources and, indeed, in all of the sources discussed in this paper.

In addition to the collimated, knotty, molecular jets, we also see H_2 shock features associated with a wide-angle wind in most of the regions. The data suggest the presence of both a collimated jet and a wide-angled wind in each Class I source. Moreover, in the Class 0 source HH 25-MMS, the H_2 knots outline a conical cavity and so poorly-collimated winds may even be associated with the youngest YSO jets. A two-component wind model for Class I and possibly even Class 0 sources is therefore preferred.

Acknowledgements. We thank Tim Carroll for his assistance with the observations, and Reinhard Mundt (the referee) for his comments and suggestions, which served to broaden and

improve the content of this paper. The *UKIRT* is operated by the Joint Astronomy Centre on behalf of the U.K. Particle Physics and Astronomy Research Council.

References

Bacciotti, F., & Eislöffel, J. 1999, A&A, 342, 717
Bacciotti, F., Mundt, R., Ray, T. P., et al. 2000, ApJ, 537, L49
Bally, J., & Devine, D. 1994, ApJ, 428, L65
Blondel, P. F. C., Talavera, A., & Djie, H. R. E. T. A. 1993, A&A, 268, 624
Bontemps, S., André, P., & Ward-Thompson, D. 1995, A&A, 297, 98
Bragg, S. L., Brault, J. W., & Smith, W. H. 1982, ApJ, 263, 999
Burton, M. G., Hollenbach, D. J., & Tielens, A. G. G. M. 1990, ApJ, 365, 620
Chernin, L. M., Masson, C. R., Gouveia dal Pino, E. M., & Benz, W. 1994, ApJ, 426, 204
Chrysostomou, A., Hobson, J., Smith, M. D., Davis, C. J., & Berndsen, A. 2000, MNRAS, 314, 229
Corcoran, M., & Ray, T. P. 1995, A&A, 301, 729
Corcoran, M., & Ray, T. P. 1998, A&A, 331, 147
Davis, C. J., Mundt, R., Ray, T. P., & Eislöffel, J. 1995, AJ, 110, 766
Davis, C. J., Ray, T. P., Desroches, L., & Aspin, C. 2001, MNRAS, 326, 524 (Paper I)
Davis, C. J., Ray, T. P., Eislöffel, J., & Corcoran, D. 1997, A&A, 324, 263
Davis, C. J., & Smith, M. D. 1995, ApJ, 443, L41
Davis, C. J., Smith, M. D., & Eislöffel, J. 2000, MNRAS, 318, 747
Downes, T. P., & Ray, T. P. 1999, A&A, 345, 977
Eislöffel, J. 2000, A&A, 354, 236
Eislöffel, J., Davis, C. J., Ray, T. P., & Mundt, R. 1994, ApJ, 422, L91
Eislöffel, J., & Mundt, R. 1992, A&A, 263, 292
Eislöffel, J., & Mundt, R. 1997, AJ, 114, 280
Eislöffel, J., Smith, M. D., & Davis, C. J. 2000, A&A, 359, 1147
Fernandes, A. J. L., & Brand, P. W. J. L. 1995, MNRAS, 274, 639
Fridlund, C. V. M., & Liseau, R. 1998, ApJ, 499, L75
Fuller, G. A., Lada, E. A., Masson, C. R., & Myers, P. C. 1995, ApJ, 453, 754
Gibb, A., & Davis, C. J. 1998, MNRAS, 298, 644
Gibb, A., & Heaton, B. D. 1993, A&A, 276, 511
Graham, J. A., & Heyer, M. H. 1990, PASP, 102, 972
Gredel, R. 1994, A&A, 292, 580
Goodrich, R. W. 1988, ApJ, 311, 882
Gueth, F., Guilloteau, S., & Bachiller, R. 1996, A&A, 307, 891
Hartigan, P., Carpenter, J. M., Dougados, C., Skrutskie, M. F. 1996, AJ, 111, 1278
Hartigan, P., Curiel, S., & Raymond, J. 1989, ApJ, 347, L31
Hartigan, P., Morse, J., Palunas, P., Bally, J., & Devine, D. 2000, ApJ, 119, 1872
Hirth, G., Mundt, R., & Solf, J. 1994a, A&A, 285, 929
Hirth, G., Mundt, R., & Solf, J. 1997, A&AS, 126, 437
Hirth, G., Mundt, R., Solf, J., & Ray, T. P. 1994b, ApJ, 427, L99
Hollenbach, D., & McKee, C. F. 1989, ApJ, 342, 306
Hollenbach, D., & Natta, A. 1995, ApJ, 455, L33
Itoh, Y., et al. 2000, PASJ, 52, 81
Johns-Krull, C. M., Valenti, J. A., & Linsky. J. L. 2000, ApJ, 539, 815
Lee, C. F., Mundy, L. G., Reipurth, B., Ostriker, E. C., & Stone, J. M. 2000, ApJ, 542, 925 (Erratum: 2001, ApJ, 549, 1231)
Lis, D. C., Menten, K. M., & Zylka, R. 1999, ApJ, 527, 856
Mitchell, G. F., Sargent, A. I., & Mannings, V. 1997, ApJ, 483, L127
Mundt, R., Ray, T. P., & Raga, A. C. 1991, A&A, 252, 740
Poetzel, R., Mundt, R., & Ray, T. P. 1992, A&A, 262, 229
Raga, A. C., & Biro, S. 1993, MNRAS, 264, 758
Raga, A. C., & Cabrit, S. 1993, A&A, 278, 267
Ray, T. P., Mundt, R., Dyson, J. E., Falle, S. A. E. G., & Raga, A. C. 1996, ApJ, 468, L103
Reipurth, B., & Aspin, A. C. 1997, AJ, 114, 2700
Reipurth, B., Yu, K. C., Heathcote, S., Bally, J., & Rodríguez, L. 2000, AJ, 120, 449
Reipurth, B., Yu, K. C., Rodríguez, L., Heathcote, S., & Bally, J. 1999, A&A, 352, L83
Shang, H., Shu, F. H., & Glassgold, A. E. 1998, ApJ, 493, L91
Shu, F. H., Ruden, S. P., Lada, C. J., & Lizano, S. 1991, ApJ, 370, L31
Shu, F. H., Najita, J., Ostriker, E. C., & Shang, H. 1995, ApJ, 455, L155
Shu, F. H., Najita, J., Shang, H., & Li, Z. Y. 2000, in Protostars and Planets IV, ed. V. Mannings, A. P. Boss, & S. S. Russell (Tucson: Univ. Arizona Press), 789
Shull, J. M., & Hollenbach, D. J. 1978, ApJ, 220, 525
Smith, M. D., & Brand, P. W. J. L. 1990, MNRAS, 242, 495
Smith, M. D., Suttner, G., & Yorke, H. W. 1997a, A&A, 323, 223
Smith, M. D., Suttner, G., & Zinneker, H. 1997b, A&A, 320, 325
Solf, J. 1987, A&A, 184, 322
Takami, H., Bailey, J., Gledhill, T. M., Chrysostomou, A., & Hough, J. H. 2001, MNRAS, 323, 177
Valenti, J. A., Johns-Krull, C. M., & Linsky, J. L. 2000, ApJS, 129, 399
Velusamy, T., & Langer, W. D. 1998, Nature, 392, 685
Völker, R., Smith, M. D., Suttner, G., & Yorke, H. W. 1999, A&A, 343, 595
Yun, J. L., et al. 2001, A&A, 372, L33